TOWARD AN ALTERNATIVE WAY OF LOOKING AT ELLIPTICAL GALAXIES: CASE STUDIES FOR NGC 4649 AND NGC 7097

V. DE BRUYNE AND H. DEJONGHE

Sterrenkundig Observatorium, Universiteit Gent, Krijgslaan 281, B-9000 Gent, Belgium; Veronique.DeBruyne@rug.ac.be

A. PIZZELLA

Osservatorio Astrofisico di Asiago, Dipartimento di Astronomia, Università di Padova, via dell'Osservatorio 8, I-36012 Asiago, Italy

M. BERNARDI

European Southern Observatory, Karl-Schwarzschild Strässe 2, D-85748 Garching, Germany; and Universitäts-Sternwarte München, Scheinerstrasse 1, D-81679 Munich, Germany

AND

W. W. ZEILINGER

Institut für Astronomie, Universität Wien, Vienna, Austria

Received 1999 November 26; accepted 2000 August 28

ABSTRACT

In this paper we consider three-integral axisymmetric models for NGC 4649 and NGC 7097, addressing the question of the presence of dark matter in these elliptical galaxies. The data for NGC 7097 can be modeled without a dark matter halo. The central region of NGC 4649 could be hosting a black hole. The kinematical data of NGC 4649 are not inconsistent with a constant mass-to-light ratio model, but a dynamical model with a moderate amount of dark matter better reproduces the observed anisotropy on the major axis. In addition, we look more closely at the issue of the classification of elliptical galaxies. Both galaxies can be placed in different families of elliptical galaxies based on the isophote shape. In this paper we set out to investigate whether the kinematic information can be used to specify a second classification parameter. We propose the use of normalized distribution functions, which are the three-integral distribution functions divided by the two-integral model (constructed from photometry alone), and argue why this is an efficient way of presenting the dynamics of elliptical galaxies. We show that they can be used to characterize the rotational state of a galaxy in a more specific way than merely indicating the amount of rotation or counterrotation. Furthermore, the distribution function for NGC 7097 suggests that the counterrotation is caused by stars spread over large radii in the galaxy, implying that this phenomenon is not related to a compact group of stars. Hence, the origin of the counterrotation should not be found in a recent merger in the first place. This shows that it is important to construct dynamic models with a distribution function. The distribution function is the tool used to visualize structure in phase space, which is the only stellar dynamic remnant of galaxy formation.

Subject headings: galaxies: elliptical and lenticular, cD — galaxies: fundamental parameters — galaxies: individual (NGC 4649, NGC 7097) — galaxies: kinematics and dynamics — galaxies: structure

1. INTRODUCTION

Our knowledge of the physical and structural properties of the stellar component of elliptical galaxies is based on the observational data retrieved from the absorption features in spectra of integrated light. For a long time, these data have been restricted to the stellar-luminosity density distribution, mean velocities, and velocity dispersions. More recently, accurate measurements of line-of-sight velocity distributions (LOSVDs) became possible. The deviations of these LOSVDs from purely Gaussian functions are expressed in terms of third- and fourth-order Gauss-Hermite coefficients (h_3 and h_4), giving additional and higher order kinematic information (see, e.g., Gerhard 1993; van der Marel & Franx 1993; Bender, Saglia, & Gerhard 1994).

The kinematic data are very important in the search for dark matter in elliptical galaxies (e.g., Bridges 1999, and references therein). At the present time, fairly extended mean velocity, velocity dispersion, h_3, and h_4 profiles are becoming available, currently up to 1–$2R_e$. The failure of a

constant mass-to-light ratio (M/L) dynamical model to fit these observed quantities is an indication of the presence of dark matter in the galaxy. In this case, the construction of models with a dark matter halo is giving an estimate for the amount of dark matter present in the galaxy.

In this paper we present models for two galaxies, NGC 4649 and NGC 7097. NGC 4649 is a luminous ($B_T = 9.77$), round galaxy with boxy isophotes from $\sim 0.12R_e$ outward, designated as E1/E2 in the Second Reference Catalogue of Bright Galaxies (de Vaucouleurs, de Vaucouleurs, & Corwin 1976), and S0$_1$ in the Revised Shaply-Ames Catalog of Bright Galaxies (Sandage & Tamman 1987, hereafter RSA). NGC 7097 is a less luminous ($B_T = 12.6$), flat galaxy, showing disky isophotes, designated as E4 in RSA and E5 in the Third Reference Catalogue of Bright Galaxies (de Vaucouleurs, de Vaucouleurs, & Corwin 1991, hereafter RC3), and having a gaseous disk (Caldwell, Kirshner, & Richstone 1986; Zeilinger et al. 1996). One of the purposes of modeling these galaxies is the question of the presence of

dark matter. The photometric and kinematic data were partly retrieved from a follow up of the ESO Key Program "A Search for Dark Matter in Elliptical Galaxies" (Bertin et al. 1989, 1994; Buson et al. 1993; Saglia et al. 1993; Zeilinger et al. 1996; Pizzella et al. 1997) and from the literature (photometry for NGC 4649: Peletier et al. 1990; photometry for NGC 7097: Sparks et al. 1991; kinematics for NGC 7097: Caldwell et al. 1986). The general properties and photometric and kinematic data that are used are summarized in Table 1.

Studies of isophote shapes, kinematic profiles (Bender 1988; Nieto et al. 1991), and axis-ratio distributions (Merritt & Tremblay 1996) indicate that the class of elliptical galaxies can be subdivided into two groups, parameterized by the well-known c_4, indicating isophote shape. We call c_4 the "first parameter."

One group of E galaxies are the more luminous ($M_V < -22.0$; Faber et al. 1997) and boxy galaxies. Based on estimates for the anisotropy parameter $(v_m/\bar{\sigma})^*$, Bender (1988) concludes that they are mostly anisotropically flattened and may be triaxial. A *Hubble Space Telescope* study of surface-brightness profiles by Faber et al. (1997) reveals that all luminous galaxies in their sample have cores, even if cuspy ones. The formation scenario is not very clear yet, but it is believed that merger processes play a dominant role in their formation history (Nieto et al. 1991; Bender & Surma 1992; Bender & Saglia 1999) making them only moderately flattened and slowly rotating and sometimes causing peculiar internal kinematics.

The other group contains the E galaxies that are less luminous ($M_V > -20.5$; Faber et al. 1997) with rather disky isophotes. They can have disks contributing modestly (a few percent up to 30%; Scorza & Bender 1995) to their total light. They are believed to be rotationally supported, and, in the sample of Faber et al. (1997), none of these galaxies have cores, but they show power-law densities continuing to the center. The assumption of oblateness seems to be adequate for modeling them. For the formation of this family of elliptical galaxies, a (non)dissipational collapse seems to suffice. If these galaxies are mergers, which cannot be excluded, significant quantities of gas should have been present and probably played an important role.

Clearly, NGC 4649 and NGC 7097 have characteristics

that place them in the first and the second group, respectively, and therefore one expects that dynamical models for both galaxies are significantly different. However, there are cases that seem to defy a classification based on the first parameter c_4; e.g., NGC 3640 is faintly boxy but is nevertheless a fast rotator $[(v_m/\bar{\sigma})^* = 1.3]$. Others, like NGC 3226, do not seem to have any clear overall value of c_4 (see Michard & Marchal 1994, and references therein). The ensuing question then is: How can dynamical modeling help to separate and map both families of elliptical galaxies?

It is well known that a variety of dynamical models can be made with the same spatial density (e.g., Dejonghe & de Zeeuw 1988; Dejonghe & Merritt 1992). Hence, a dynamical model clearly provides additional information that is not included in the photometry. This is a trivial statement to the degree that a dynamical model provides a picture of the orbital structure of the galaxy, which is obviously not contained in the photometry. In this paper, however, we set out to explore another possible use of dynamical models: as discriminants for further and more detailed classification. More particularly, the issues we want to clarify are the following: (1) Is the kinematic information available sufficient to decouple a dynamical model from the information already contained in the photometry? (2) How does one extract in a relatively simple or straightforward way a "second parameter" from a dynamical model?

In order to answer the first question, we want to look at whether there are any significant differences between the distribution functions that can be attributed to the kinematic data alone. Since it clearly does not make sense to produce a model that uses kinematics alone and disregards the photometry, we need to normalize our models somehow to the effect of eliminating the photometric information. Therefore, we will present our three-integral models after dividing them with an even two-integral model that reproduces the photometry. In this way we will be able to study the effects of the kinematics on the three-integral structure of the model.

The data reduction for the Key Program is described in § 2. The dynamical modeling was performed using a quadratic-programming technique developed by Dejonghe (1989); the basic principles can be found in § 3. In that section we also give an outline of the deprojection and the modeling procedure that we adopt for the two galaxies. We present the models for NGC 4649 and NGC 7097 in § 4. The normalization of the models is explained in § 5. In that section we also present a comparison of both models by means of the normalized distribution functions and a discussion on the counterrotation in NGC 7097. Section 6 sums up and concludes.

2. OBSERVATIONS AND DATA REDUCTION

NGC 4649 and NGC 7097 were observed with the ESO 3.5 m New Technology Telescope (NTT) using the ESO Multi Mode Instrument (EMMI). The observing log is given in Table 2. EMMI was used in the Dichroic Medium Dispersion spectroscopy configuration. In this paper we present only the results obtained from the red-arm data. Long-slit spectra were obtained with grating 6 centered on $\lambda = 5150$ Å covering a wavelength region of 540 Å with a dispersion of 28 Å mm^{-1}. The detector employed is a Thompson 1024×1024 pixel CCD (ESO CCD 18) with a pixel size of 19×19 μm. The CCD was rebinned to 4×4

TABLE 1

GENERAL PROPERTIES AND PHOTOMETRIC DATA FOR NGC 4649 AND NGC 7097

Parameter	NGC 4649	NGC 7097
B_T	9.77[a]	12.6[e]
M_V	−22.13[b]	−21.2[f]
Distance (Mpc)	26.7[c]	52[g]
Effective radius	82″ ($\approx$ 10 kpc)[c]	19″.3 ($\approx$ 5 kpc)[g]
Morphological type	E1/E2	E4/E5
Isophotes	Boxy[d]	Some disky[f,h]
Dust	...	Some dust[h]

NOTE.—B_T is total blue magnitude.
[a] Burstein et al. 1987.
[b] Faber et al. 1997.
[c] van der Marel 1991.
[d] Peletier et al. 1990.
[e] RC3.
[f] Sparks et al. 1991.
[g] Caldwell et al. 1986.
[h] Buson et al. 1993.

TABLE 2

LOG OF OBSERVATIONS CARRIED OUT AT THE 3.5 M NTT

Name	P.A. (deg)	Date	Exposure Time (minutes)	Notes
NGC 4649...	15	1992 May 29	60	Minor axis
	15	1992 May 29	60	
	105	1992 May 30	60	Major axis
	105	1992 May 30	60	
	105	1992 May 31	37	
	105	1992 May 31	60	
NGC 7097...	15	1992 May 30	60	Major axis
	15	1992 May 30	58	
	15	1992 May 31	60	
	15	1992 May 31	60	
	15	1992 May 31	53	
	15	1992 May 31	60	

pixels yielding an effective scale of 1″.76 pixels^{-1} and effective dispersion of 2.1 Å pixel^{-1} using a slit width of 3″. We derived an instrumental dispersion of about 90 km s^{-1} by measuring the line width of the thorium calibration spectra.

Each galaxy spectrum was bracketed by two thorium calibration spectra in order to correct for instrument flexure effects. Stellar templates were observed in the same instrument configuration. The stellar-template spectra have been taken moving the star across and along the slit several times (basically by means of a zig-zag movement). The final spectrum, which has been used for measuring the kinematics, is the average of all the spectra obtained this way.

The spectra were calibrated using standard procedures for bias and dark-current subtraction and flat-fielding within the MIDAS software package. Cosmic-ray events were corrected using a median-filter algorithm. After wavelength calibration, the single spectra along major and minor axes were aligned and combined, respectively. Sky subtraction was then performed using the edge of the CCD uncontaminated by galaxy light. The spectra were rebinned along the spatial direction in order to achieve a constant signal-to-noise ratio of about 20. The calibrated spectra were first analyzed using the Fourier correlation quotient technique (Bender 1990; Bender et al. 1994), yielding radial-velocity and velocity-dispersion profiles together with h_3 and h_4 profiles. The results were confirmed using the Fourier quotient technique (e.g., Bertola et al. 1984; Pizzella 1996).

2.1. Derived Kinematics for NGC 4649

The data derived for the major and minor axes are presented in Figure 1. The kinematic data extend out to 100″ (12.9 kpc = $1.2R_e$) along both the major and minor axes. The mean velocity and velocity-dispersion profiles are symmetric with respect to the center. Along the major axis the velocity rises up to 100 km s^{-1} at the last measured point. The velocity dispersion is 400 km s^{-1} in the center and decreases to 200 km s^{-1} in the last measured point. The value of h_3 is slightly positive in the center (~ 0.05) and becomes about 0 for $r > 3.9$ kpc; h_4 is about 0 in the center and becomes negative for $r > 3.9$ kpc.

Along the minor axis the velocity rises slowly to a value of about 30 km s^{-1} in the outer region. The nonzero veloc-
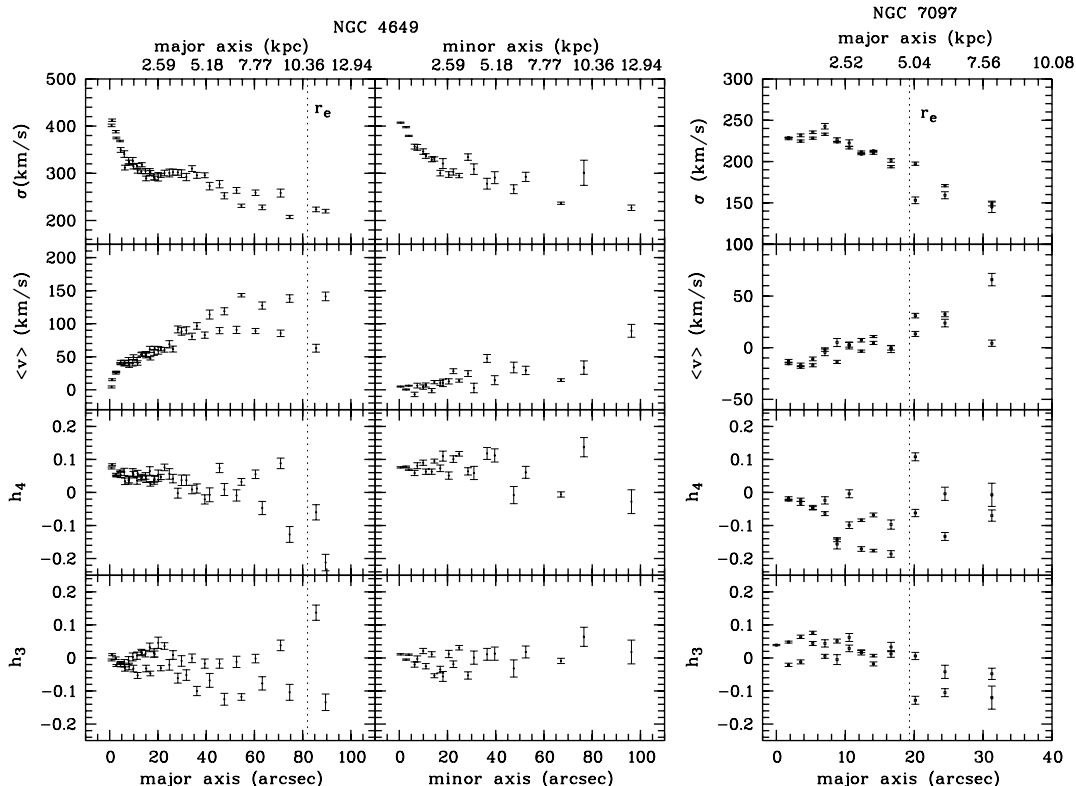

FIG. 1.—Kinematic data derived from the observations. The left-hand panels show the velocity dispersion, the mean velocity, h_3, and h_4 for the major and minor axis of NGC 4649. The right-hand panel shows the same quantities for the major axis of NGC 7097. The vertical dotted lines indicate the effective radius on the major axis.

ity might be due to a slightly triaxial shape of the galaxy (this is the boxy galaxy of our sample), but the rotation remains much less than the velocity dispersion. The velocity dispersion is 400 km s^{-1} in the center (in agreement with the major axis measurement) and drops down to 200 km s^{-1} at the last measured point. The value of h_3 is about 0, while h_4 is about 0.1 at all radii.

2.2. *Derived Kinematics for NGC 7097*

The kinematic data for the major axis (also shown in Fig. 1) extend out to $r = 30''$ (7.5 kpc = 1.6R_e) and are symmetric about the center. We find evidence of a kinematically decoupled core as the rotational velocity reaches -20 km s^{-1} at a distance of $r = 3''.5 = 0.88$ kpc from the center. We interpret this as a signature for a central component in counterrotation with the main body of the galaxy. This is discussed in more detail in § 5.2. From $r = 3''.5 = 0.88$ kpc on, the mean velocity decreases outward, being 0 at $r = 7'' = 1.76$ kpc, changing sine and reaching about 40 km s^{-1} at the last measured point. The velocity dispersion measured in the center is 230 km s^{-1}, increases slightly to 240 km s^{-1} at $r = 1.76$ kpc, then decreases to 100 km s^{-1}. The value of h_3 is slightly positive (about 0.05) and becomes negative for $r > 1R_e$. The value of h_4 is almost 0 in the center and decreases to about -0.1 outward.

The maximum velocity dispersion in correspondence with $r = 1.76$ kpc is due to the presence of the two counterrotating components. In fact, at that radius the two components are contributing equally to the galaxy light, so that the mean velocity is 0 and the velocity dispersion is high. As expected at this radius, we also find $h_3 \sim 0$ and $h_4 < 0$. In the external region stars rotate in the same direction as the ionized gas disk.

3. OUTLINE OF THE MODELING TECHNIQUE

The internal motions of a galaxy can be described using a distribution function $F(r, z)$ in phase space. Modeling the dynamic structure of a galaxy is equivalent to the construction of such a distribution function. This requires the knowledge of the potential of the system, which is derived in part from the luminous-mass density (LMD). The LMD is obtained through a deprojection of the observed photometry.

For both the deprojection and the construction of a distribution function, we use a quadratic-programming method (Dejonghe 1989). In general terms, it is assumed that the solution of the problem is a function G that consists of a number of basis functions of a chosen form, with an appropriate coefficient for each:

$$G = \sum_i c_i G_i . \qquad (1)$$

In order to find a suitable linear combination of basis functions, a χ^2-like variable is constructed. This variable is essentially

$$\chi^2 = \sum_l \text{weight}_l[\text{moment}(x)_{\text{observed}} - \text{moment}(x)_{\text{calculated}}]^2 , \qquad (2)$$

and contains all observable moments of the function that are considered in the fit. The summation contains each data point l that is included in the fit; with x we denote the coordinates of the point where the data is taken. The inclusion of the weight function makes it possible to differentiate

between the importance of several moments. The values for c_i are found through minimization of this χ^2, while extra linear constraints on the final solution G can be included. One of the most important constraints is the nonnegativity of the function. This general technique is adopted for two different problems—the deprojection of the luminosity profile and the construction of a distribution function.

3.1. *The Deprojection*

For the deprojection problem, we use basis functions for the LMD of the form

$$G_i(\varpi, z) = \exp\left[\frac{-\sqrt{\varpi^2 + (z/q)^2}}{\sigma,}\right], \qquad (3)$$

where σ and q are the parameters of the library of components. We try to construct a function for the LMD that gives the best fit to the observed photometric profile after projection. In the general expression for χ^2 in equation (2), moment (x) stands for the surface brightness measured in (x, y), a point in the image of the galaxy projected on the sky. These basis functions have the same parameters as the ones used by Emsellem, Monnet, & Bacon (1994).

3.2. *The Distribution Function*

In this paper we assume that distribution functions can be three-integral distribution functions. An approximation for such a third integral I_3 can be analytically calculated if spheroidal coordinates are used, which allows us to use a potential in Stäckel form. It is important to note that the Stäckel form of the potential is used only when it is necessary to calculate I_3; in all other cases we use the potential obtained from the deprojection.

The distribution function is a linear combination of Fricke-type components, depending on three integrals of motion:

$$G_i(E, I_2, I_3) = E^p I_2^q (I_2 + I_3)^n , \qquad (4)$$

where $2I_2 = L_z^2$ and I_3 is an approximate third integral. The parameters p and q can be real; n is an integer. A more detailed description of the construction of a distribution function with these components can be found in Dejonghe et al. (1996). A typical model is made using a library that contains ~ 400–500 components.

For the determination of the distribution function, we make use of all available observables. In the expression for χ^2 in equation (2) the sum of weighted moments contains the photometric profile, the mean velocity, and velocity dispersion. Also, h_3 and h_4 are included where available.

The expression for the third- and fourth-order Gauss-Hermite moments is as follows:

$$h_l = 2\sqrt{\pi}\mu_0 \int \exp\left(-\frac{x^2}{2\sigma^2}\right)H_l(x)\mathscr{L}(v)dv , \qquad (5)$$

with

$$x = \frac{\langle v \rangle - v}{\sigma} . \qquad (6)$$

Herein $\langle v \rangle$ and σ are the observed mean velocity and velocity dispersion in the points where h_3 or h_4 are calculated. $H_l(x)$ is the third- or fourth-order Gauss-Hermite polynomial, and $\mathscr{L}(v)$ is the line profile. The expressions in equation (5) with $l = 3$ or $l = 4$ are linear functions in the

distribution function. This makes it possible to include them in our quadratic-programming method.

4. THE CASE OF NGC 4649 AND NGC 7097

4.1. *The Photometry and the Deprojection*

4.1.1. *NGC 4649*

The photometry of NGC 4649 was taken from Peletier et al. (1990). We performed a deprojection adopting a 90° inclination of the rotation axis with respect to the line of sight (edge-on). The difference between the original photometric profile and the obtained LMD projected on the plane of the sky is always smaller than 0.02 mag. The expression for the LMD is a sum of 21 components of the type indicated in equation (3). Figure 2 shows the contours of the projected LMD (*solid lines*) that are almost completely overlapped by the original profile (*dotted lines*) in the left-hand panel and the contours for the LMD in the right-hand panel (*solid lines*).

4.1.2. *NGC 7097*

We took the photometric profiles from Sparks et al. (1991). Also, for NGC 7097, the deprojection is performed assuming the galaxy is seen edge-on. Based on the presence of the gaseous disk, an inclination of about 60° could be envisaged, as suggested by Caldwell et al. (1986) and Zeilinger et al. (1996). However, this would imply a flattening of the E4/E5 galaxy that is too large to be realistic. Moreover, the misalignment of the gaseous disk with the stellar isophotes may indicate that it is inclined with respect to the equatorial plane, which probably makes it unsuitable as an indicator of the inclination. The difference between the original photometry and a projection of the LMD (a sum of 18 components) nowhere is larger than 0.03 mag. In Figure 2 we show the isophotes of the projected LMD (*dashed lines*) and the original photometry (*dotted lines*) in the left-hand panel; the LMD is shown in the right-hand panel (*dashed lines*).

4.2. *The Fit*

The data and observations we are taking into account for the modeling are the mass density, the photometry, the mean velocity $\langle v \rangle$, the velocity dispersion σ, and the third- and fourth-order Gauss-Hermite moments.

For both galaxies, we constructed a set of 11 models. The set consists of (1) a model based on the photometry and kinematics as they were observed and (2) 10 models, each based on a different artificially created kinematic data set that is statistically indistinguishable from the original data set given the error bars. The photometry is kept the same, however. Hence, we get an indication of the way the model changes if it is based on another data set that lies within the errors. Moreover, we obtain a Monte Carlo estimate of the errors on the models.

4.2.1. *NGC 4649*

NGC 4649 was included in the sample of Faber et al. (1997) for the study of the centers of early-type galaxies. They estimated an $(M/L)_V = 16.2$, based on a Nuker law fit to the brightness profile, with M/L assumed to be constant and an isotropic velocity dispersion.

The derivation of the kinematic data (i.e., the mean velocity and velocity-dispersion profiles on major and minor axes together with h_3 and h_4) is discussed in § 2. For the data we used in the fit, we averaged the observed values in the corresponding points at a positive and negative radius along the axes.

4.2.1.1. Constant M/L Model

The dynamical model consists of 43 components. Figure 3 shows the difference between the original surface brightness and the model surface brightness, while the velocity dispersion, the mean velocity, and the higher order Gauss-Hermite moments are displayed in Figure 4. For the photometric profiles, the mean value for the set of models is shown. For the mean velocity and the velocity-dispersion profiles, the mean is shown together with the 2 σ bounds. The profiles for the model based on the real observed data are very similar to the mean. For the Gauss-Hermite moments, the mean of the set of models is shown (*solid line*) together with the results for the model based on the real observed data (*open stars*). Filled stars appear where both overlap.

The dispersion profiles are well fitted on both axes (see left-hand panels of Fig. 4) except for the central points where the velocity dispersion rises very quickly toward the center. Our models are not hot enough in that region to reproduce the high values, which may indicate an increase in M/L inward from 10″ (1.29 kpc). This is also an explana-
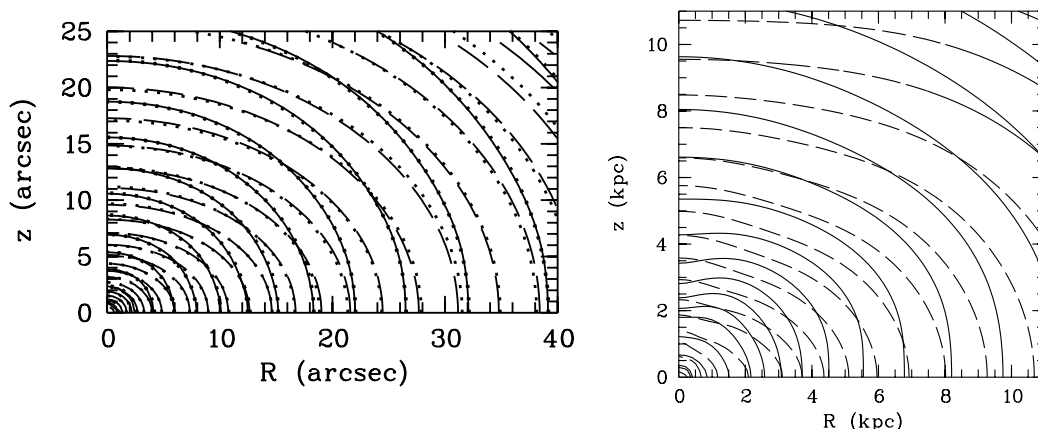

FIG. 2.—*Left-hand panel*: The contours for the LMD projected on the plane of the sky for NGC 4649 (*solid lines*) and for NGC 7097 (*dashed lines*). For both galaxies, the contours of the original photometry are overplotted in dotted lines. *Right-hand panel*: The contours for the LMD for NGC 4649 (*solid lines*) and NGC 7097 (*dashed lines*). The LMD for NGC 7097 is clearly the most flattened.
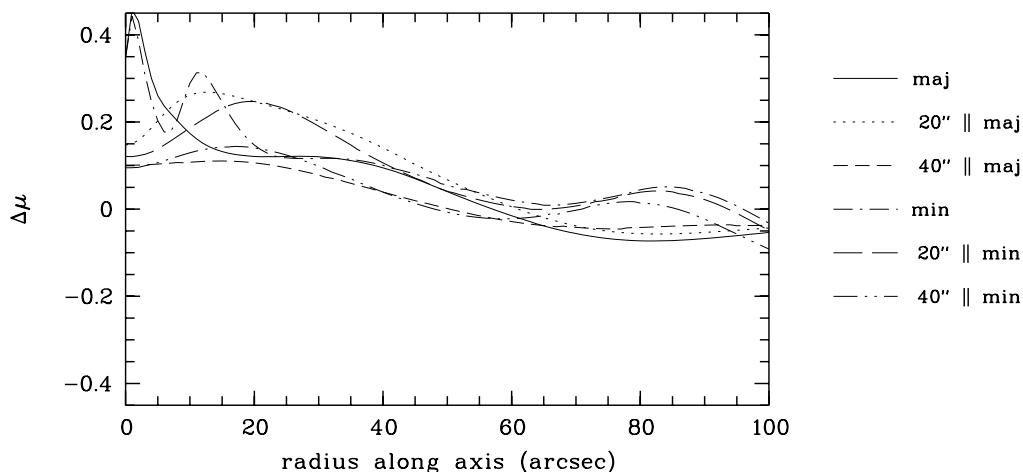
FIG. 3.—NGC 4649. The difference between the original surface brightness and the model surface brightness along several radii. *Solid line*: major axis. *Dotted line*: axis at 20″ parallel to the major axis. *Short-dashed line*: axis at 40″ parallel to the major axis. *Dash-dotted line*: minor axis. *Long-dashed line*: axis at 20″ parallel to the minor axis. *Dash–double-dotted line*: axis at 40″ parallel to the minor axis.

tion for the rather large difference between the observed surface brightness and the model surface brightness in the inner pixels (~ 0.4) on major and minor axes. The model wants to get enough mass to fit the central velocity-dispersion profile and tries to get it from lowering the surface brightness a bit. This could indicate the presence of a black hole, but our data lack the spatial resolution necessary for a more thorough analysis.

The fits to the higher order Gauss-Hermite moments (right-hand panels of Fig. 4) are harder to judge because both sides of the slits appear to be somewhat inconsistent and there is a large spread on the measurements, especially in the outer parts. For all profiles, the general tendency is reproduced, but there are a number of data points that are not fitted.

4.2.1.2. Model with Dark Matter Halo

Since the model with constant M/L does suggest that the fit on h_4 can be improved, especially on the major axis, we also considered a dynamical model with a dark matter halo. This model is a sum of 41 components. The amount of dark

matter is assumed to grow linearly with radius, and at 13 kpc from the center about 90% of the total mass is contained in the luminous mass.

The results on the photometry with this model are very similar to the results of the model without dark matter. Figure 5 shows the fit to the kinematical data. For the fit to the velocity dispersion and mean velocity, the same remarks as for the constant M/L model can be made. For the higher order Gauss-Hermite moments, we obtained a good fit on the major axis. It is clear that the inclusion of a modest amount of dark matter resulted in smoother profiles compared to the constant M/L model. However, on the minor axis, the fit to h_4 is definitely worse than in the constant M/L case. For the comparison of the distribution functions of NGC 4649 and NGC 7097, we will use the dark matter model, but our conclusions hold for the constant M/L model as well.

4.2.2. NGC 7097

The gas and star kinematics of NGC 7097 were studied by Caldwell et al. (1986). They found a gas disk that is
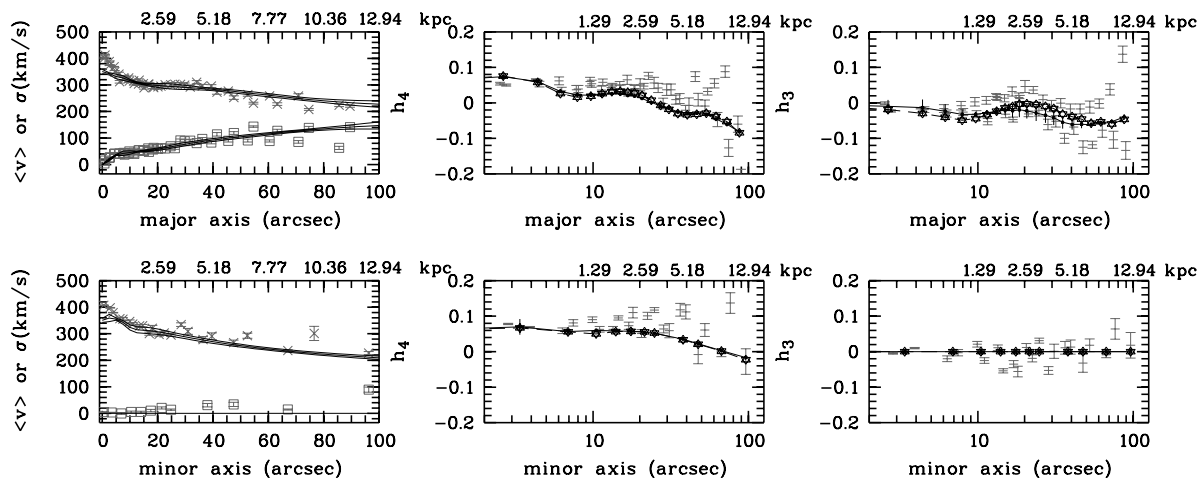

FIG. 4.—Constant M/L model for NGC 4649. The upper row shows profiles along the major axis; the lower row shows profiles along the minor axis. *Left-hand panels*: the mean velocity and velocity-dispersion profiles (mean and 2 σ curves) are plotted together with the data. *Middle and right-hand panels*: the means and σ for h_4 and h_3, respectively. The data are plotted in horizontal lines; the mean of the fits is shown as solid lines, with σ displayed as error bars; the results of the model based on the real observed data are shown as stars (and the points are connected with a dashed line).
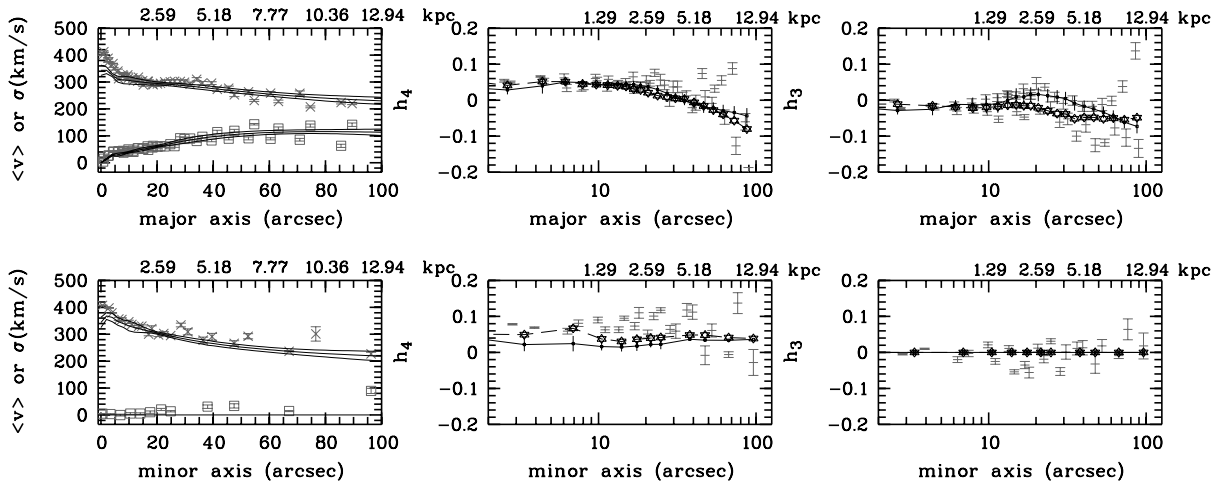
Fig. 5.—Model with dark matter for NGC 4649. The upper row shows profiles along the major axis; the lower row shows profiles along the minor axis. *Left-hand panels*: the mean velocity and velocity-dispersion profiles (mean and 2 σ curves) are plotted together with the data. *Middle and right-hand panels*: the means and σ for h_4 and h_3, respectively. The data are plotted in horizontal lines; the mean of the fits is shown as solid lines, with σ displayed as error bars; the results of the model based on the real observed data are shown as stars (and the points are connected with a dashed line).
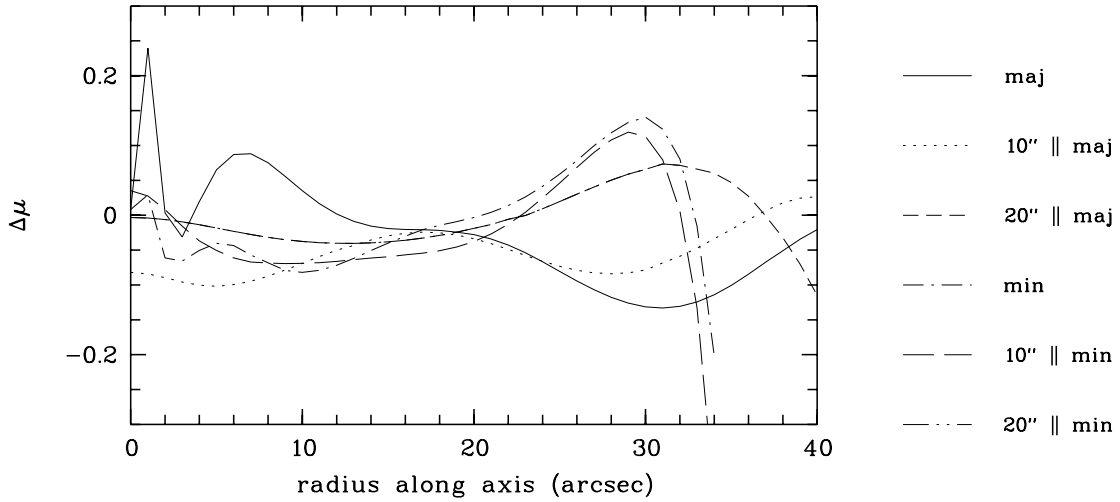

Fig. 6.—NGC 7097. The difference between the original surface brightness and the model surface brightness along several radii. *Solid line*: major axis. *Dotted line*: axis at 10″ parallel to the major axis. *Short-dashed line*: axis at 20″ parallel to the major axis. *Dash-dotted line*: minor axis. *Long-dashed line*: axis at 10″ parallel to the minor axis. *Dash–double–dotted line*: axis at 20″ parallel to the minor axis.
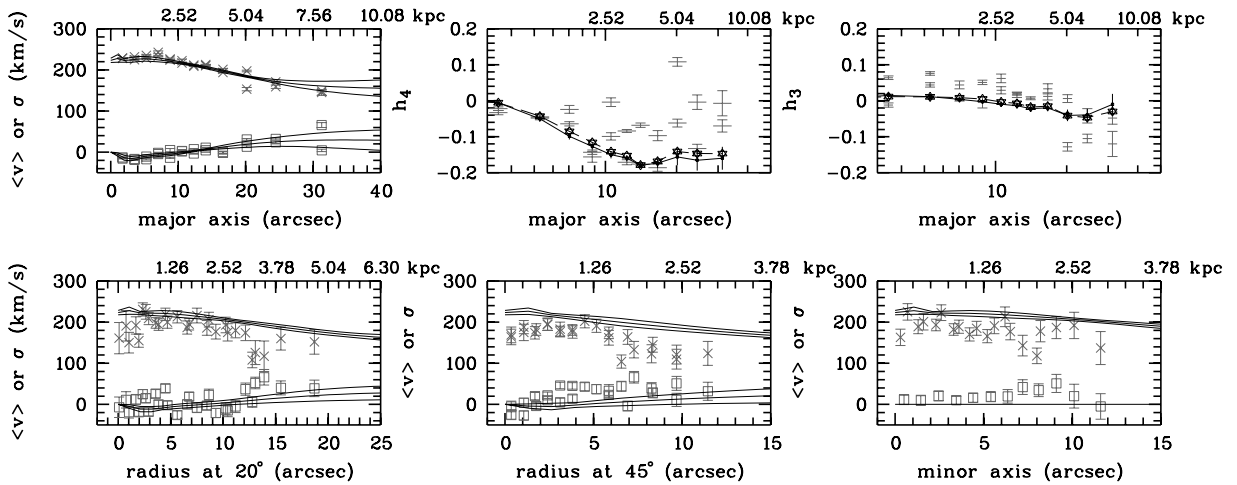

Fig. 7.—Model for NGC 7097. The mean and the 2 σ deviation level are shown for the major axis (*upper left-hand panel*), the axis tilted at 20° (*lower left-hand panel*), the axis tilted at 45° (*lower-middle panel*), and the minor axis (*lower right-hand panel*). *Upper-middle and right-hand panels*: the fit to h_4 and h_3 on the major axis. The data are plotted in horizontal lines, and the mean of the fits is shown as solid lines, with σ displayed as error bar; the results of the model based on the real observed data is shown as stars (and the points are connected with a dashed line).

aligned with the major axis and reported that gas and stars are in counterrotation. The assumption of circular gas velocities leads to a nonconstant M/L, which indicates the presence of dark matter if a variation in the stellar composition can be ruled out. The spherical models they constructed using a linear-fitting method indicate that the radial component is larger than the tangential dispersion.

In a later study the presence of a gas disk is confirmed (Zeilinger et al. 1996), but it appears to be misaligned by about $30°$ with the stellar isophotes. The modeling of the ionized-gas velocity field using a triaxial potential (Pizzella et al. 1997) gave no indication for the presence of dark matter; a constant $(M/L)_B = 8$ was found. Derivation of the mass distribution for the inner region by Bertola et al. (1993) indicated a constant $(M/L)_B = 5$ up to $\sim 0.9 R_e$.

The observations reported in this paper resulted only in major axis data for this galaxy, i.e., the mean velocity and velocity-dispersion profiles together with values for h_3 and h_4. Additional kinematic information was retrieved from the literature. Caldwell et al. (1986) obtained mean-velocity profiles and velocity-dispersion profiles along four slits: major and minor axes and two axes through the center, tilted at $20°$ and $45°$. Their data extend up to about $1R_e$; this means that they do not really provide additional information regarding the presence of dark matter, but they can be useful in order to determine the internal kinematic structure of the galaxy. The mean velocity on the minor axis is very small, not violating the assumption of axisymmetry. The data points were taken at each side of the center, but the assumed axisymmetry of the galaxy allows us to average the measured kinematics at corresponding distances along both sides of the center; they are shown in Figure 7.

The two data sets are not completely compatible, as can be seen easily when comparing the values for the central velocity dispersion. We measured 228 km s^{-1}, while the values from Caldwell et al. (1986) are much lower (~ 160 km s^{-1}). The velocity-dispersion profile from our observations is in good agreement with the values presented by Carollo, Danzinger, & Buson (1993). On the major axis there is a fairly good agreement between both data sets. When fitting the data points, we cannot expect that both sets will be equally well fitted, and we will assign more weight to our data.

The dynamical model for NGC 7097 is constructed with 28 components. The difference between the original surface brightness and the model surface brightness is shown in Figure 6. We show the results of the fits to the derived kinematical data and the data of Caldwell et al. (1986) in Figure 7. The fit to the velocity dispersion, presented by the mean and the $2\,\sigma$ deviation levels (*upper left-hand and lower panels*), is very good on the major axis. For the other axes, the rather poor fit to these data essentially can be explained by the fact that the central values for the velocity dispersion at these axes are not compatible with the measurements on the major axis. The model is able to reproduce the counterrotation in the inner part. The profiles for the model based on the real observed data are not shown since they are very similar to the mean.

For the third- and fourth-order Gauss-Hermite moments, the quality of the fit is satisfying (Fig. 7, *upper right-hand panels of*), as well for the mean of the set of models (*solid line*) and the model based on the real observed data (*stars*). One might argue that some of the data points are not well represented. On the other hand, the spread on the measured

values makes it almost impossible to fit all data points with a smooth profile.

5. THE NORMALIZED MODELS

5.1. *The Signature of the Kinematics*

As already mentioned in § 1, we aim to separate the effects of the photometry and velocity dispersion in our distribution functions. The idea is to divide the three-integral distribution function obtained through a fit to the photometry and the full kinematic data set by the even two-integral distribution function that is determined completely by fitting the photometry.

Moreover, from a physical point of view, it is interesting to note that the normalized distribution function $G(E, L_z, I_3) = F_{3I}/F_{2I}$ is dimensionless and coordinate independent:

$$\frac{F_{3I}(\boldsymbol{r}, \boldsymbol{v})d\boldsymbol{r}\,d\boldsymbol{v}}{F_{2I}(\boldsymbol{r}, \boldsymbol{v})d\boldsymbol{r}\,d\boldsymbol{v}} = \frac{F_{3I}(\boldsymbol{r}', \boldsymbol{v}')\left|\dfrac{\partial(\boldsymbol{r}, \boldsymbol{v})}{\partial(\boldsymbol{r}', \boldsymbol{v}')}\right|d\boldsymbol{r}'d\boldsymbol{v}'}{F_{2I}(\boldsymbol{r}', \boldsymbol{v}')\left|\dfrac{\partial(\boldsymbol{r}, \boldsymbol{v})}{\partial(\boldsymbol{r}', \boldsymbol{v}')}\right|d\boldsymbol{r}'d\boldsymbol{v}'} . \quad (7)$$

It is useful to compare the normalized distribution functions $G(E, L_z, I_3)$ for both galaxies. The even two-integral that are used for the normalization are presented in Appendix A.

We show intersections with the plane $I_3 = 0$ in Figure 8. In the left-hand panels we present contour plots of $\langle \log (G) \rangle$, with angle brackets denoting the mean of the 11 models, in the (E, L_z) plane. The energy is scaled to the total depth of the potential well. The distribution functions are considered within the same energy interval $[E', 1]$. The angular momenta L_z are scaled to $(L_c)_{max}$, corresponding to the angular momentum of the circular orbits with energy E'. In the right-hand panels of Figure 8 we present $\langle \log (G) \rangle$ in turning-point space $[\sin (L_z)R_-, R_+]$, restricted to the region where kinematic data are available. Here R_+ is the apocenter in the equatorial plane, R_- is the pericenter in the equatorial plane, and the sine of R_- is equal to the sine of L_z.

For all four contour plots, positive values denote a relative overdensity compared to the two-integral model, and negative values indicate similarly relative underdensities. We checked that all over- and underdensities are significant (i.e., above 2 σ) as long as the over- or underdensity is larger than 0.05.

Obviously, one should not attach any meaning to the fact that the galaxy has a total z-angular momentum that is negative since this depends on the choice of the axes. In our convention counterrotation is produced by orbits with positive L_z.

Although the same quantity (the intersection of the normalized distribution function with the plane with $I_3 = 0$) is shown twice for both galaxies in Figure 8, the figures give complementary information. The presentation in the (E, L_z)–plane gives a clear view on the presence of radial orbits, while circular orbits are compressed. For the plot in turning-point space, the opposite holds.

The representation in the (E, L_z)–plane of the distribution for the boxy galaxy NGC 4649 clearly stresses the importance of orbits with small $|L_z|$ (a large positive region over almost all E around the axis $L_z = 0$ in the upper left-hand panel of Fig. 8). They represent the radial or near radial orbits. The highest values for the contours (>0.8) can be
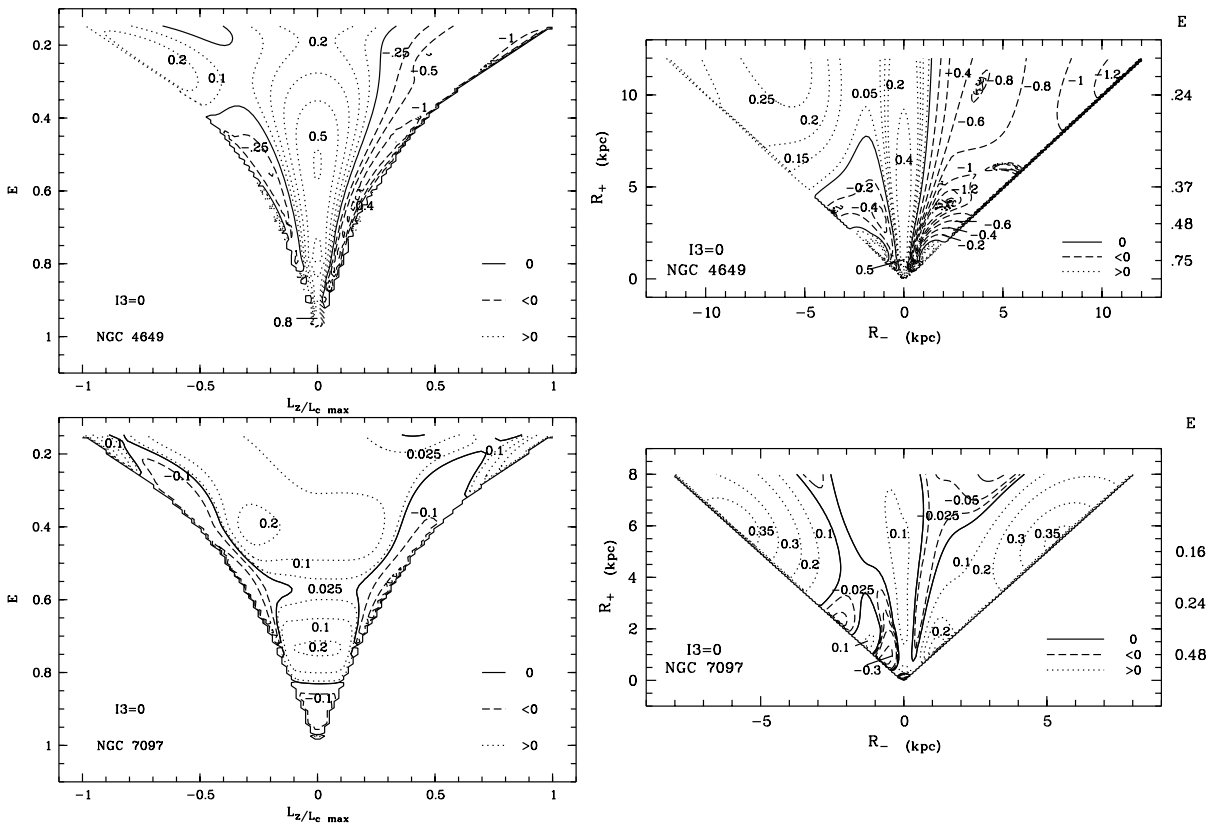
Fig. 8.—Intersection of $\langle \log (G) \rangle$ with the plane $I_3 = 0$ for NGC 4649 (*upper panels*) and for NGC 7097 (*lower panels*). The left-hand panels present the intersection in the (E, L_z)–plane; the right-hand panels present the same intersection in turning-point space. R_+ is the apocenter in the equatorial plane; R_- is the pericenter in the equatorial plane; the sine of R_- is equal to the sine of L_z. Values for E, the energy of the circular orbit with the corresponding radius, are indicated at the right-hand border of the figures. For all four panels, the zero-contours are in full. Dashed lines indicate negative values, and dotted lines correspond to positive contours.

found for orbits not too far from the center, with $R_+ < 0.4$ kpc. This overdensity is entirely due to the additional information contained in the kinematics and has nothing to do with the photometry. There is also a region with positive contours for $E < 0.38$ or $R_+ > 4.7$ near the border for negative L_z, indicating a preference for circular and near-circular orbits with negative angular momentum. This overdensity is even clearer in the representation in turning-point space (upper right-hand panel of Fig. 8). The panel also shows a small relative overdensity for circular or almost circular orbits with positive L_z ($0.95 < R_- < 1.9$), indicating that a small amount of counterrotating orbits is consistent with the observed mean-velocity profile.

The representation of the distribution function for NGC 7097 in the (E, L_z)–plane (lower left-hand panel of Fig. 8) shows positive contours in a central region that are almost symmetric and that have broad wings. This indicates that for every E, there is a large range in values for L_z, e.g., for $E = 0.4$, $-0.39 < L_z/L_{c \, max} < 0.35$, while the maximum value for that value of E is $|L_z/L_{c \, max}| = 0.5$, and for $E = 0.7$, the maximum value for $|L_z/L_{c \, max}| = 0.19$, while the distribution function has values for $|L_z/L_{c \, max}|$ between 0 and 0.15.

This region also contains radial orbits, but this type of orbit is not as important for any value of E as is the case in NGC 4649. For NGC 4649, the radial orbits close to the center are mostly populated, while for NGC 7097, an underdensity is found in that region. The prevalence of orbits with large angular momentum (positive contours at the edges of

the lower right-hand panel of Fig. 8) is more obvious in the representation in turning-point space. The orbits with positive angular momentum (right-hand edge of the figure) are used to create the counterrotation.

In order to make the significance of these overdensities and underdensities clear, both distribution functions can be compared. To make this somewhat easier, we use the following diagnostic:

$$\eta = \frac{\langle \log (G_{\mathrm{NGC} \, 4649}) \rangle - \langle \log (G_{\mathrm{NGC} \, 7097}) \rangle}{2 \sqrt{\sigma_{\mathrm{NGC} \, 4649}^2 + \sigma_{\mathrm{NGC} \, 7097}^2}}, \qquad (8)$$

with angle brackets and σ the mean and the dispersion of $\log (G)$ of 11 models. The two normalized distribution functions are considered to be significantly different if $|\eta| > 1$, i.e., if their logs differ by more than the 2 σ error estimate.

A contour plot for the comparison of planes with $I_3 = 0$ is shown in Figure 9. The contours for the values -1, 0, and 1 are shown as solid lines. The dashed and dotted lines show regions where the normalized distribution functions are significantly different. They fill the (E, L_z)-plane almost completely. The dashed lines indicate negative contours; the normalized distribution function for NGC 4649 reaches significantly lower values than the normalized distribution function for NGC 7079 in these regions. The opposite holds for the regions with dotted lines.

This figure clearly shows that purely kinematic information (mainly velocity dispersion but also mean velocity and higher order Gauss-Hermite moments) (1) contains addi-
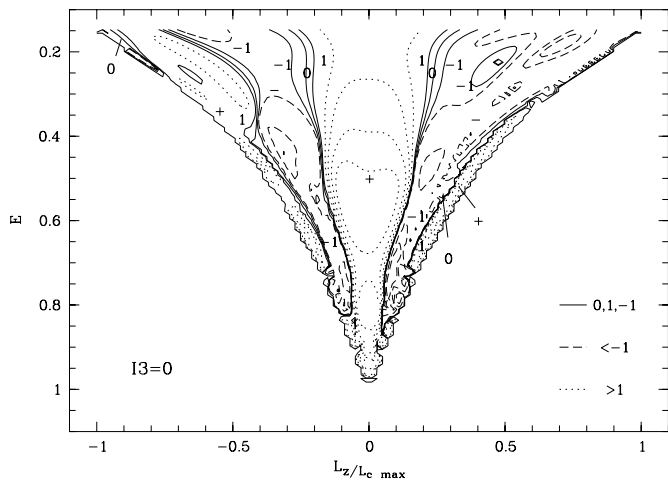
FIG. 9.—Comparison of the normalized distribution functions in the $I_3 = 0$–plane. The contours for the values -1, 0, and 1 are shown as solid lines. Dashed lines indicate negative values ($f_{\mathrm{NGC\,7097}} > f_{\mathrm{NGC\,4649}}$), and dotted lines are for positive contours ($f_{\mathrm{NGC\,4649}} > f_{\mathrm{NGC\,7097}}$).

tional information that is not present in the photometry and (2) has a sufficiently large signal that it can be used as an additional discriminant.

There are three conclusions: (1) The dotted contours in the central region (small $|L_z|$) indicate that the orbital density of radial orbits is significantly high for the models of the boxy NGC 4649. (2) The models of NGC 4649 contain more circular orbits than the normalized models of NGC 7097. (3) Two off-center regions with dashed contours (one with $L_z > 0$ and one with $L_z < 0$) indicate that moderate to high values for L_z are favored in the models for NGC 7097. We note in particular that the prevalence of radial orbits in NGC 4649 is *not* due to the boxy photometry. The kinematics of NGC 7097 imply a surplus of rotation in comparison to the kinematics of NGC 4649.

Given the fact that there is no obvious alternative for showing the signature of the kinematics in dynamical models, we suggest that a second structure parameter for elliptical galaxies could be derived from the diagnostic η. However, our comparison of only two galaxies has too limited a scope in order to lead to a more specific suggestion.

5.2. Counterrotation in NGC 7097

Intrinsically peculiar velocity fields, such as, e.g., counter-rotating cores, are found more frequently in boxy ellipticals than in disky ellipticals (e.g., Mehlert et al. 1998, and references therein). They are believed to be a natural byproduct of the merging of star-dominated systems, which seems to be the most plausible formation scenario for luminous boxy galaxies (Bender & Saglia 1999). Moreover, the decoupled cores also have enhanced metallicities compared to the main body (Bender & Surma 1992; Carollo & Danziger 1994). The difference in metallicity between the core and main body is also used to argue that the merging occurred between very few objects with similar mass instead of dissipationless merging of a compact elliptical with a more luminous object or accretion of gas-rich companions and subsequent star formation.

As for disky E galaxies, NGC 1700 is the only system with a counterrotating core studied in great detail so far;

Franx, Illingworth, & Heckman (1989) measured $\langle v \rangle_{\min} \sim -25$ km s^{-1}. More recent observations (Statler, Smecker-Hane, & Cecil 1996) and modeling (Statler, Dejonghe, & Smecker-Hane 1999) indicate that the counterrotation has only weak influence on the kinematics. Studying stellar kinematic fields, Statler et al. (1996) conclude that NGC 1700 could also be formed by a merger of stellar systems. Carollo et al. (1997) found a hint for a slightly redder inner structure and even slightly boxy isophotes on the scale of the counterrotating core.

Figure 10 shows a representation of the distribution function in turning-point space where the number of corotating orbits is subtracted from the number of counterrotating orbits. Positive contours indicate that in that region the model contains more orbits with positive L_z (producing counterrotation) than orbits with negative L_z.

In the upper panel one can easily see the prevalence of orbits with $L_z < 0$ in the case of NGC 4649. The middle panel shows the distribution function for NGC 7097, where
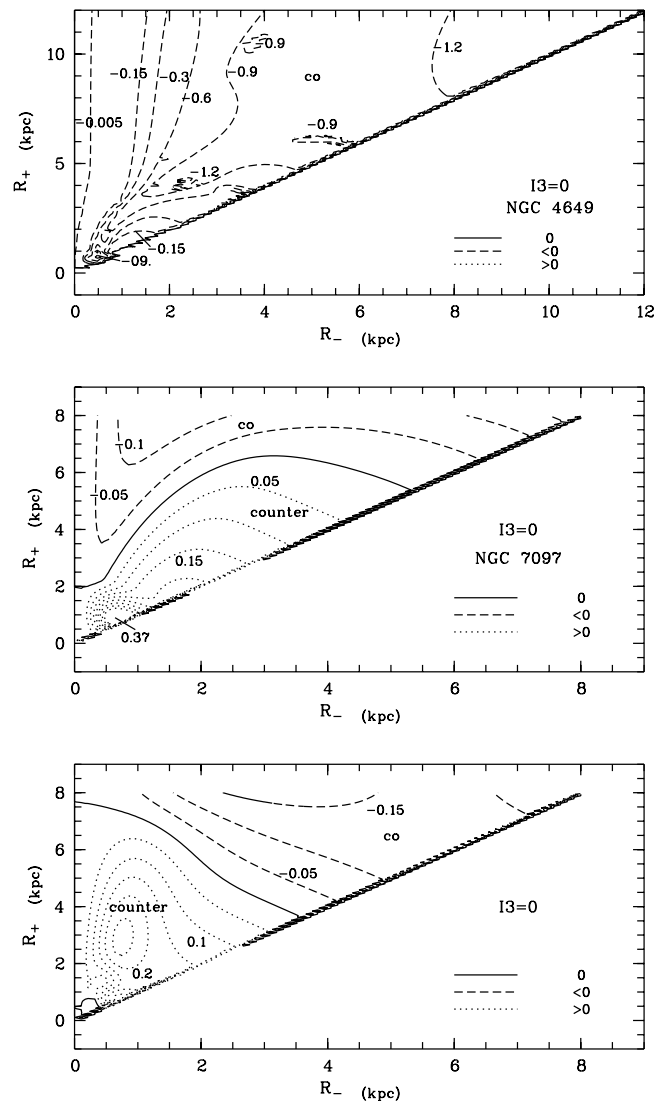

FIG. 10.—Normalized distribution function for $I_3 = 0$, where the number of orbits with $L_z < 0$ is subtracted from the number of orbits with $L_z > 0$ for NGC 4649 (*upper panel*) and NGC 7097 (*middle panel*). The lower panel shows the distribution function from modeling photometry and dispersion profiles just like NGC 7097, but with more mean rotation and more counterrotation ($\langle v \rangle$ between -40 km s^{-1} and 40 km s^{-1}).

a large number of orbits with positive L_z are present. For these orbits, $0 < R_-, R_+ < 5.5$ kpc; they are present in the galaxy at large distances from the center ($1R_e \simeq 5$ kpc). This shows that the signal in $\langle v \rangle$ (with values between -20 km s^{-1} and 20 km s^{-1}; see Fig. 7) is not sufficient to trace back the counterrotation to a group of orbits in a limited area of space. The highest values for the contours are found in the region close to the center, approximately where the lowest $\langle v \rangle$ is measured.

For the calculation of the projected mean velocity at a radius R, all orbits with an apocenter larger than R are involved. These orbits can be found above the horizontal line at distance R from the center in the plot for the distribution function in turning-point space. For the distribution function of NGC 7097, a region with negative contours lies close to the R_+ axis, spread over a large range in R_+. This means that for the calculation of the projected mean velocity, there is always an amount of counterrotating orbits and an amount of corotating orbits involved, this is also the case in the region where the observed $\langle v \rangle$ is negative. This indicates that the number of counterrotating orbits there is large enough to account for the observed counterrotation, even if a number of corotating orbits do also contribute. For larger radii, where the observed mean velocity is positive (for $r > 1.76$ kpc), there also apparently is no problem in mixing corotating and (a fairly large amount of) counterrotating orbits.

This situation is somewhat similar to what is seen in NGC 4550 (S0/E7), where about one-half of the stars in the principal plain are on prograde orbits, while the other half of the stars are on retrograde orbits, with the two disks extending over a sizable portion of the galaxy (Rubin, Graham, & Kenney 1992; Kuijken, Fisher, & Merrifield 1996). Both components appear to be kinematically cold and very similar, and therefore the situation in NGC 4550 is very different from the counterrotating cores found in elliptical galaxies (Rix et al. 1992).

As an illustration, the lower panel of Figure 10 shows the distribution function from a toy galaxy with the same photometry and dispersion profiles as NGC 7097 but with twice the counterrotation ($\langle v \rangle$ has values between -40 and 40 km s^{-1}). With these data, the region with the counterrotating stars is better confined and more limited in space. We see that there is no region with negative contours near the R_+-axis (contrary to the distribution function of NGC 7097, see middle panel); the corotating orbits all have pericenters larger than 4 kpc. In this case, the projected velocity in the region where negative $\langle v \rangle$ is observed is calculated using almost only counterrotating orbits. For larger radii, positive projected velocities are obtained using mainly corotating orbits. The amount of rotation (positive and negative) in the observed mean-velocity profile does not seem to allow a relevant mixing of co- and counterrotating orbits. Therefore, this situation is in large contrast with the model of NGC 7097.

The results for NGC 7097 and the toy model indicate the following:

1. The distribution function of a dynamical model can tell whether the observed counterrotation in a galaxy is caused by a compact group of stars or not. The amount of rotation and counterrotation in the mean-velocity profile is important. The fact that NGC 7097 does not have much rotation on the one hand and that there is not much

counterrotation on the other hand allows us to distribute counterrotating orbits over the galaxy to beyond $1R_e$. A model with more rotation and more counterrotation does not allow considerable mixing of orbits with positive and negative L_z.

2. Counterrotation is not automatically linked to a recent merger event where the components have not mixed up yet. Also, a dissipationless merging of a compact object is ruled out as possible formation scenario (Kormendy 1984; Balcells & Quinn 1990). As an alternative, one could think of gas infall followed by star formation. There is indeed a gas disk in NGC 7097 (Caldwell et al. 1986; Zeilinger et al. 1996), but it is misaligned with the stars, and it rotates in the same direction as the outer stars. This makes it not very plausible, however, that the counterrotating stars would have formed out of the gas disk.

Another possible scenario is formation by a single dissipationless collapse, which can produce counterrotation cores (Barnes & Efstathiou 1987; Harsoula & Voglis 1998). Also, an old merger event, followed by tidal interactions that caused the spread of the counterrotating stars, could be a possible scenario in this case.

6. RESULTS AND CONCLUSIONS

6.1. Dark Matter in NGC 4649 and NGC 7097?

Based on the major- and minor-axis kinematical data (out to about $1.2R_e$) used in this paper, a three-integral constant $(M/L)_V = 9.5$ model for NGC 4649 cannot be simply rejected. However, a dynamical model with a moderate amount of dark matter—about 10% at 13 kpc ($1.2R_e$)—yields a better fit to h_4 on the major axis. For both models, the velocity dispersion in central regions is not well fitted because the inclusion of some dark matter is required. The photometry and kinematics of NGC 7097, out to $1.6R_e$, can be well fitted with a three-integral constant $(M/L)_V = 7.2$ model. For both galaxies, the models have a realistic degree of anisotropy in the velocity-dispersion tensor.

6.2. Kinematics as Additional Classification Parameter

If a second parameter for the classification of elliptical galaxies is to be found, a parameter based on the kinematics is an obvious candidate. However, an important constraint is that such a second parameter should be independent from the first. This is not trivial because up to now photometry and kinematics have always been used as one data set in the production of the models and in the presentation of the results of these models.

A first step is to disentangle the influence of photometry and kinematics on the obtained models. We do this by constructing what we call a normalized presentation, which is the three-integral model, based on all observable information, divided by the two-integral model determined by the photometry. Such a presentation (1) only carries the signature of the mean velocity, velocity dispersion, and higher order Gauss-Hermite moments because it is independent of the spatial density distribution and (2) has an absolute meaning since it is coordinate independent. An intersection of the normalized distribution functions with a plane of $I_3 = 0$ shows that one can make a distinction between dynamical models on the basis of the kinematic information alone.

The normalized presentations show that the kinematics of NGC 4649 lead to a dark matter model with a large

amount of radial or near-radial orbits and also where circular or near-circular orbits come to the fore. The kinematics of NGC 7097 lead to models where intermediate values for L_z, within a fairly large range, are favored. These results also hold when the constant M/L models are compared.

We suggest that studying normalized distribution functions could be a very useful way to find a second structure parameter based on the kinematic information alone. However, a larger sample of models is needed to come to a more specific suggestion for such a parameter.

6.3. *Counterrotation in NGC 7097*

NGC 7097 is one of the very few ellipticals with regular isophotes where a counterrotating core is observed. This galaxy is also peculiar for another reason; it is very flattened (E4/E5), and yet there are not many galaxies that flat and with that little rotation.

Our dynamical modeling showed that the amount of counterrotation in NGC 7097 is not sufficient to conclude that it is caused by a spatially confined group of stars.

Instead, the counterrotating stars are spread all over the galaxy. This implies that a small amount of counterrotation combined with a small amount of rotation is not necessarily the result of a (recent) merger. The example of a model with more counterrotation and more rotation shows that the resulting distribution function can be used to make the distinction between cases that favor a compact group of counterrotating stars and cases with counterrotating stars on orbits spread over the galaxy.

Our conclusion that the counterrotation in NGC 7097 probably is not caused by a compact group of stars cannot be reconciled with the generally accepted idea that peculiar cores reside in luminous galaxies and are the result of a merger of stellar systems with comparable mass. There are two possible ways to explain this: either the picture for the formation of kinematically decoupled cores is not complete yet or NGC 7097 is simply a problematic case because it is too peculiar. In both cases, the modeling of a larger number of ellipticals with counterrotating cores can be clarifying.

APPENDIX

THE EVEN MODELS

The normalization of the three integral model uses a two-integral distribution function that is determined by photometry alone. The modeling technique is the same as for the three-integral models (§ 3) but now uses Fricke components (see § 4) with $n = 0$. The two-integral models have the same mass as the corresponding three-integral models. For NGC 4649, we used 10 components for the even model. For NGC 7097, the model is made with 12 components. Figure 11 shows these models. The middle panels show intersections of the distribution functions with the $I_3 = 0$–plane (*left-hand panels*) and the distribution functions in turning-point space (*right-hand panels*). The contours in these panels are very regular. This ensures that the
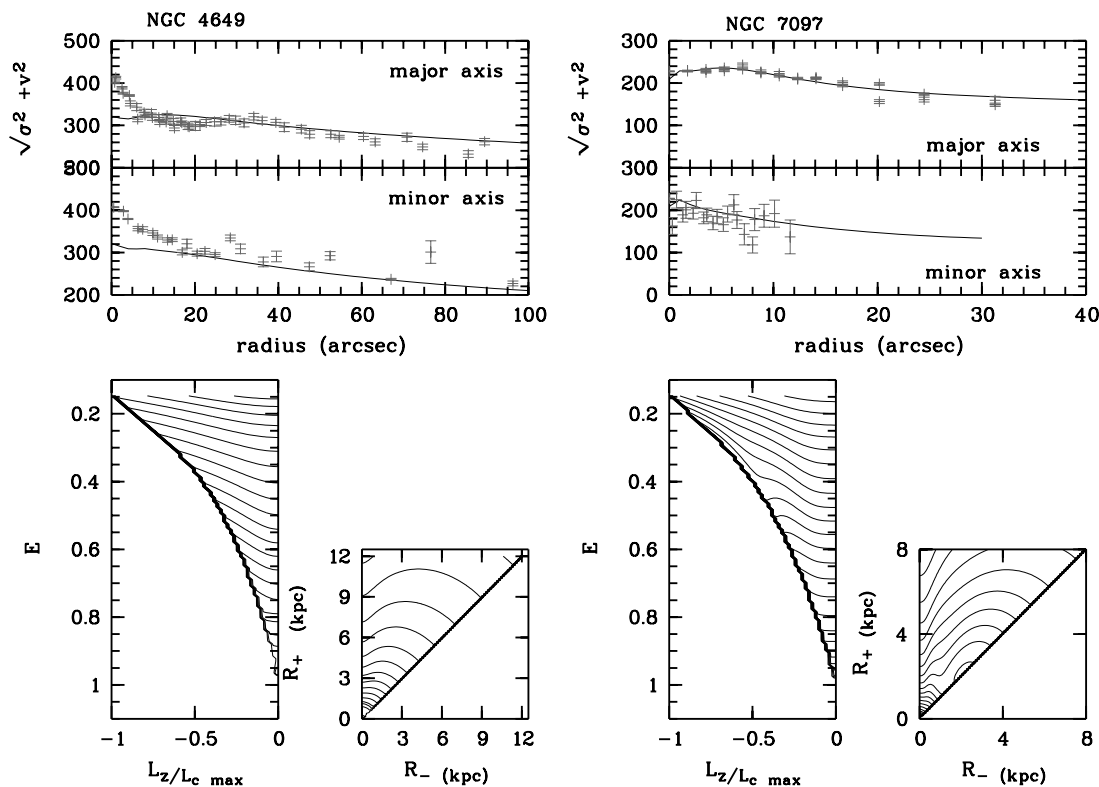

Fig. 11.—Even distribution functions for NGC 4649 (*left-hand panel*) and NGC 7097 (*right-hand panel*). *Upper panels*: predictions for the second-order moments along major and minor axis. *Lower left-hand panel*: intersections of the distribution function with planes of constant I_3. *Lower right-hand panel*: the distribution function in turning-point space.

normalizations are done using a smooth function. Therefore, the impact of the normalization on the small scale structure of the normalized models is small.

REFERENCES

Balcells, M., & Quinn, P. 1990, ApJ, 361, 381
Barnes, J., & Efstathiou, G. 1987, ApJ, 319, 575
Bender, R. 1988, A&A, 193, L7
———. 1990, A&A, 229, 441
Bender, R., Saglia, R. P. 1999, in ASP Conf. Ser. 182, Galaxy Dynamics ,
    ed. D. R. Merritt, J. A. Sellwood, & M. Valluri (San Francisco: ASP), 113
Bender, R., Saglia, R. P., & Gerhard, O. E. 1994, MNRAS, 269, 785
Bender, R., & Surma, P. 1992, A&A, 258, 250
Bertin, G., et al. 1989, Messenger, 56, 19
———. 1994, A&A, 292, 381
Bertola, F., Bettoni, D., Rusconi, L., & Sedmark, G. 1984, AJ, 89, 356
Bertola, F., Pizzella, A., Persic, M., & Salucci, P. 1993, ApJ, 416, L45
Bridges, T. 1999, in ASP Conf. Ser. 182, Galaxy Dynamics, ed. D. R.
    Merritt, M. Valluri, & J. A. Sellwood (San Francisco: ASP), 415
Burstein, D., Davies, R. L., Dressler, A., Faber, S. M., Stone, R. P. S.,
    Lynden-Bell, D., Terlevich, R., & Wegner, G. 1987, ApJS, 64, 601
Buson, L., et al. 1993, A&A, 280, 409
Caldwell, N., Kirshner, R. P., & Richstone, D. O. 1986, ApJ, 305, 136
Carollo, C. M., & Danziger, I. J. 1994, MNRAS, 270, 523
Carollo, C. M., Danziger, I. J., & Buson, L. 1993, MNRAS, 265, 553
Carollo, C. M., Danziger, I. J., Rich, R. M., & Chen, X. 1997, ApJ, 491, 545
Dejonghe, H. 1989, ApJ, 343, 113
Dejonghe, H., De Bruyne, V., Zeilinger, W. W., & Vauterin, P. 1996, A&A,
    306, 363
Dejonghe, H., & de Zeeuw P. T. 1988, ApJ, 333, 90
Dejonghe, H., & Merritt, D. 1992, ApJ, 391, 531
de Vaucouleurs, G., de Vaucouleurs, A., & Corwin, H. G. 1976, Second
    Reference Catalogue of Bright Galaxies (Austin: Univ. Texas Press)
———. 1991, Third Reference Catalogue of Bright Galaxies (New York:
    Springer)

Emsellem, E., Monnet, G., & Bacon, R. 1994, A&A, 285, 723
Faber, S. M., et al. 1997, AJ, 114, 1771
Franx, M., Illingworth, G., & Heckman, T. 1989, ApJ, 344, 613
Gerhard, O. E. 1993, MNRAS, 265, 213
Harsoula, M., & Voglis, N. 1998, A&A, 335, 431
Kormendy, J. 1984, ApJ, 287, 577
Kuijken, K., Fisher, D., & Merrifield, D. 1996, MNRAS, 283, 543
Mehlert, D., Saglia, R. P., Benderm R., & Wegner, G. 1998, A&A, 332, 33
Michard, R., & Marchal, J. 1994, A&AS, 105, 481
Merritt, D., & Tremblay, B. 1996, AJ, 111, 2243
Nieto, J.-L., Poulain, P., Davoust, E. & Rosenblatt, P. 1991, A&AS, 88, 559
Pizzella, A. 1996, Ph.D. thesis, Univ. Rome
Pizzella, P., et al. 1997, A&A, 323, 349
Peletier, R. F., Davies, R. L., Illingworth, G. D., Davis, L. E., & Cawson,
    M. C. 1990, AJ, 100, 1091
Rix, H.-W., Franx, M., Fisher, D., & Illingworth, G. 1992, ApJ, 400, L5
Rubin, V. C., Graham, J. A., & Kenney, J. D. 1992, ApJ, 394, L9
Saglia, R. P., Bertin, G., Bertola, F., Danziger, I. J., Sadler, E. M., Stiavelli,
    M., de Zeeuw, P. T., & Zeilinger, W. W. 1993, ApJ, 403, 567
Sandage, A. R. & Tamman, G. 1987, A Revised Shaply-Ames Catalog of
    Bright Galaxies (2d ed; Washington: Carnegie Inst.) (RSA)
Scorza, C., & Bender, R. 1995, A&A, 293, 20
Sparks, W. B., Wall, J. V., Jorden, P. R., Thorne, D. J., & Van Breda, I.
    1991, ApJS, 76, 471
Statler, T. S., Dejonghe, H., & Smecker-Hane, T. 1999, AJ, 117, 126
Statler, T. S., Smecker-Hane, T., & Cecil, G. N. 1996, AJ, 111, 1512
van der Marel, R. P. 1991, MNRAS, 253, 710
van der Marel, & R. P., Franx, M. 1993, ApJ, 407, 525
Zeilinger, W. W., et al. 1996, A&AS, 120, 257